ASME Journal of Biomechanical Engineering
Online journal at:
https://asmedigitalcollection.asme.org/biomechanical

Surface Reaction of Electroosmotic Flow-Driven Free Antigens With Immobilized Magnetic-Microbeads-Tagged-Antibodies in Microchannels

Israel O. Ajiboye
Mem. ASME
Department of Mechanical and Materials Engineering,
University of Cincinnati,
Rhodes Hall 601, 2851 Woodside Drive,
Cincinnati, OH 45219
e-mail: ajiboyio@mail.uc.edu

Rupak K. Banerjee[1]
Mem. ASME
Department of Biomedical Engineering,
University of Cincinnati,
Veterans Affairs Medical Center,
Rhodes Hall 593, 2851 Woodside Drive,
Cincinnati, OH 45219
e-mail: banerjr@ucmail.uc.edu

Immunoassays based on reactions between target pathogen (antigen; Ag) and antibody (Ab) are frequently used for Ag detection. An external magnetic field was used to immobilize magnetic microbeads-tagged-antibodies (mMB-Ab) on the surface of a microchannel in the capture zone. The mMB-Ab was subsequently used for Ag detection. The objective of this numerical study, with experimental validation, is to assess the surface reaction between mMB-Ab and Ag in the presence of electro-osmotic flow (EOF). First, immobilization of mMB-Ab complex in the wall of the capture zone was achieved. Subsequently, the Ag was transported by EOF toward the capture zone to bind with the immobilized mMB-Ab. Lastly, mMB-Ab:Ag complex was formed and immobilized in the capture zone. A finite volume solver was used to implement the above steps. The surface reaction between the mMB-Ab and Ag was investigated in the presence of electric fields (E): 150 V/cm–450 V/cm and Ag concentrations: 0.001 M–1000 M. The depletion of mMB-Ab increases with time as the E decreases. Furthermore, as the concentration of Ag decreases, the depletion of mMB-Ab increases with time. These results quantify the detection of Ag using the EOF device; thus, signifying its potential for rapid throughput screening of Ag. This platform technology can lead to the development of portable devices for the detection of target cells, pathogens, and biomolecules for testing water systems, biological fluids, and biochemicals.
[DOI: 10.1115/1.4065138]

Introduction

Every year, millions of people worldwide suffer from diseases caused by harmful microbial infections [1]. As a result, rapid, precise, and early detection of bacteria is critical in a variety of applications, such as drug discovery involving screening assays, food and water safety analysis [2,3], and biosensing [4,5], including disease diagnostics [6,7]. Traditional methods for bacteria detection involve intricate methods, leading to a time-consuming process, causing them to be unsuitable for field testing. In contrast, direct bacteria identification on-site can be quick and inexpensive and can be done using a portable instrument. Polymerase chain reaction and its derivatives, loop-mediated isothermal amplification, mass spectrometry, etc., have demonstrated promise in identifying bacteria without using traditional bacterial cultures when coupled with microfluidic devices [8,9]. Microfluidic devices, which miniaturize numerous laboratory processes, have shown promise in the development of diagnostic immunoassays for rapid identification of pathogens [10–12]. Magnetophoretic separation, which uses magnetic microbeads (mMBs) tagged with antibodies (Ab) for identifying antigens (Ag) of interest, is one of these immunoassay techniques.

Magnetophoretic Separation. Magnetophoretic-based immunoassay—a well-known technique—employs mMBs coated with binding ligands that attach to specific biomolecules, allowing the mMB complex to be extracted from the system [13]. The mMBs are made of iron oxide nanospheres (Fe_2O_3 or Fe_3O_4) embedded in a polystyrene substrate [14]. Several experimental and numerical investigations have been conducted to improve the capture efficiency (CE), the ratio of captured beads to all beads in the system, of mMBs. Min et al. [15] isolated quantum-dot-attached circulating tumor cells (CTC) using anti-IgG-modified mMBs, reporting a CE of 70–80%. Similarly, Lu et al. [16] isolated and detected CTCs in blood samples from 17 cancer patients using biotin-triggered decomposable mMBs, and 2–215 CTCs were identified with high purity. You et al. [17] utilized gold nanoparticle-coated starch mMBs to effectively separate and target E. coli from an aqueous solution.

Electro-Osmotic Flow. The mMBs can be driven either by pressure [18,19] or electrohydrodynamic flow [20–22] such as EOF. The EOF has advantages in microfluidics as it (1) does not require

[1]Corresponding author.
Manuscript received January 3, 2024; final manuscript received March 14, 2024; published online April 8, 2024. Assoc. Editor: Nicole Hashemi.

mechanical pumps operating at higher pressures [14,23,24] that is prone to leakage and (2) is inexpensive and efficient when operating at small volumes (nanoliters) while providing improved flow and directional control. The EOF is driven by an external electric field (E) under atmospheric conditions where the flowrate is directly proportional to the applied E across charged microchannels. The E is achieved by placing electrodes in the inlet and outlet reservoirs and by applying a voltage potential across the microchannel. Selmi and Belmabrouk [25] investigated the effects of alternating current EOF on the transport and binding reaction in a heterogeneous immunosensor of C-reactive protein Ag with its corresponding Ab anti-C-reactive protein construct. Kaziz et al. [26] performed a numerical analysis to determine the impact of EOF on the reaction kinetics of the SARS-CoV-2 S protein binding. They reported an optimal binding reaction when a pair of electrodes were placed on the bottom wall of the microchannel, facing the reacting surface.

Magneto-Electro-Osmotic Flow. Electro-osmotic flow is utilized to drive mMBs in the microchannel because it offers greater flexibility in adjusting the magnitude and the direction of the flow by varying the E in the microchannel. Alipanah et al. [27] developed an EOF-driven magnetophoretic microfluidic device to separate magnetic particles from human blood. They reported that on-chip separation is possible for particles with sizes between 100 nm and 2.5 μm by altering the strength of the magnetic field and E. Similarly, Deraney et al. [28] designed an EOF-based microfluidic device for extracting nucleic acids bound to mMBs. They reported a 15% increase in DNA extraction with EOF compared to without EOF. A prior numerical study conducted by our lab, Das et al. [14], reported enhanced CE of mMBs using a combination of reduced magnetic field and sequentially switched EOF, a novel concept. Similar microfluidic studies by Das et al. [22] and Miller et al. [29], leading to a patent (Banerjee et al. [30]), used EOF and fluorescent microscopy to capture quantifiable mMBs.

Reaction With Magneto-Electro-Osmotic Flow. The microfluidic device discussed above was tested for improved capture of mMB-E. coli* (here, * indicates fluorescent tagged E. coli for optical detection) complexes using the patented method of sequentially switching of EOF [29,31]. Even though devices with different microchannel designs have been developed to capture Ag with mMB-Ab, investigation of the surface reaction of immobilized mMB-Ab with free Ag in presence of magneto-EOF physics has not been reported before. The present study is an important and necessary extension of our recent past studies.

The magneto-EOF microfluidic device in this study is developed for *high throughput screening* having *reusability*. This device is reusable multiple times following release of mMB complex after demagnetization or removal of magnet; therefore, microchannel surfaces can be cleaned of mMB complexes and reused, reducing time and cost. Typically, this microfluidic device can be used as a first step in a field condition prior to detailed and more accurate testing in a lab setting.

The *objective* of this study is to formulate and conduct numerical analyses of immobilized mMB-Ab and free Ag reaction in the presence of EOF while validating results with experimental data [23] obtained in our lab. It is *hypothesized* that the immobilized mMB-Ab and free Ag exposed to variable E will allow rapid and improved detection of Ag. The steps for the numerical formulation are discussed in the following methodology section.

Methodology

Figure 1(*a*) shows the schematic diagram of the proposed device. First, the mMBs are tagged with the antibodies (Ab) outside the channel to form mMB-Ab. Subsequently, the mMB-Abs get injected into the microchannel from the inlet reservoir. During this first step, the mMB-Abs are immobilized at the wall of the microchannel by an external magnetic field. After the mMB-Abs have been captured and immobilized on the channel wall, the antigen (Ag) gets injected into the channel as a second step from the inlet and is captured by the immobilized functional mMB-Ab forming mMB-Ab:Ag at the microchannel wall of the capture zone. These sequential steps were reported in our previous experimental study.

Geometry. The two-dimensional domain, shown in Fig. 1(*b*), comprises a miniaturized permanent magnet (150 μm × 150 μm) and a charged microchannel (length: 2 mm and height: 100 μm). It consisted of an 800 μm long capture zone (Figs. 1(*b*) and 1(*c*)), where mMB-Ab was immobilized and available to bind with Ag. The inlet (0 mm) of the microchannel to 0.6 mm is the section before the capture zone. The capture zone starts from 0.6 mm (leading edge) and ends at 1.4 mm (trailing edge) and beyond that is the rest of the channel. At the inlet and outlet of the microchannel, a positive and negative electrode was placed. Thus, an E is generated, which results in the generation of an EOF.

Governing Equations

Electro-osmotic Flow. The following equations of EOF were derived based on Krishnamoorthy et al. [32] and Comandur et al. [23]

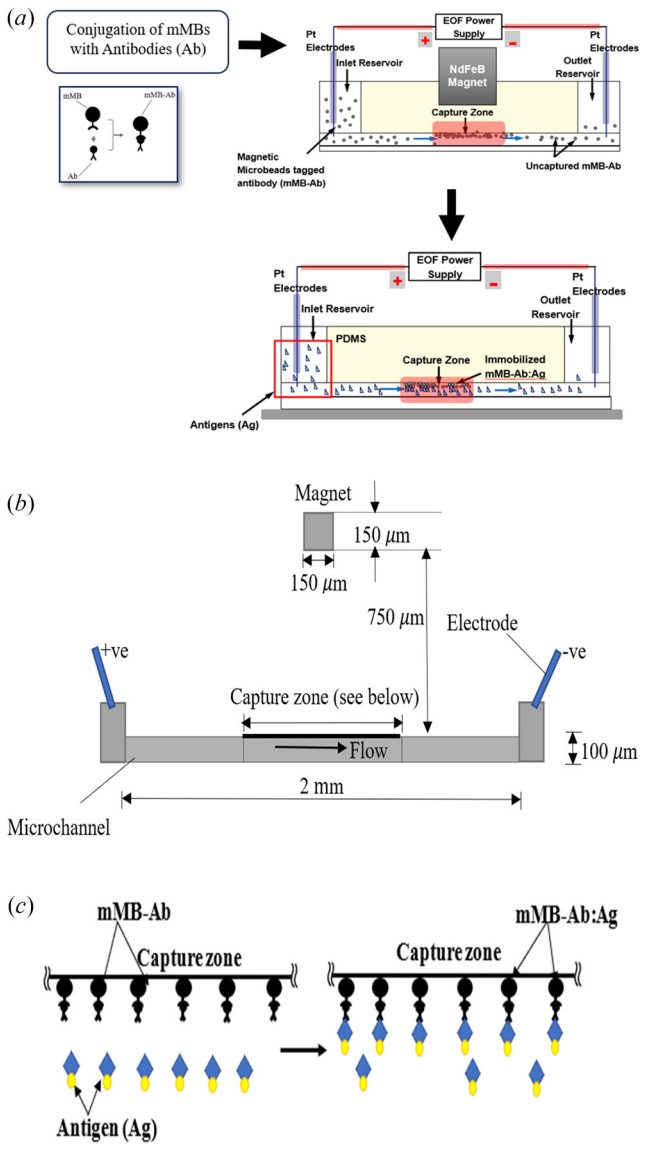

Fig. 1 Schematic diagram of (*a*) microfluidic device, (*b*) microchannel with capture zone, and (*c*) capture of Ag with immobilized mMB-Ab in capture zone

$$\text{Conservation of mass}: \nabla.\boldsymbol{V} = 0 \tag{1}$$

$$\text{Conservation of momentum}: \rho D\boldsymbol{V}/Dt = -\nabla p + \mu\nabla^2\boldsymbol{V} + f_e \tag{2}$$

$$\text{Coulomb force}: f_e = \rho_e \boldsymbol{E} \tag{3}$$

$$\text{Poisson's equation}: \nabla^2\varphi = 0 \tag{4}$$

$$\text{Electric field}: E = -\nabla\varphi \tag{5}$$

where $\boldsymbol{V}$ represents the fluid velocity, ρ is the fluid density, μ is dynamic viscosity, φ is the applied potential, ρ_e is the bulk charge, and $\boldsymbol{E}$ is the applied electric field. The momentum equation (Eq. (2)) includes the Coulomb force (Eq. (3)) exerted by the external E. Since $\rho_e = 0$, the Coulomb force term is zero. The flow equations are coupled with E at the boundary, even though the bulk charge is zero. The pressure drop term is zero because a constant pressure was maintained at the inlet and outlet of the channel during EOF. Poisson's equation (Eq. (4)) was then coupled with the momentum equation (Eq. (2)). The E in the channel was solved using Eq. (5).

Magnetophoretic Flow. The governing equations for the magnetic field, velocity, and the magnetic force experienced by mMB-Ab are presented below (Das et al. [14])

$$\text{Magneto} - \text{static equation}: \boldsymbol{M} = \frac{\boldsymbol{B}}{\mu_0\mu_r}(\mu_r - 1) \tag{6}$$

$$\text{Magnetic force on mMB} - \text{Ab}: \boldsymbol{F_m} = \frac{1}{2\mu_0}\chi\left(\frac{4}{3}\pi {r_b}^3\right)(\boldsymbol{B}\nabla)\cdot\boldsymbol{B} \tag{7}$$

$$\text{Drag force on mMB} - \text{Ab}: \boldsymbol{F_d} = 6\pi\mu r_b(\boldsymbol{V} - \boldsymbol{v_b}) \tag{8}$$

Newton's 2nd law (force balance on mMB-Ab)

$$\left(\frac{4}{3}\pi {r_b}^3\rho_b\right)\frac{d\boldsymbol{v_b}}{dt} = \boldsymbol{F_m} + \boldsymbol{F_d} + \boldsymbol{F_g} + \boldsymbol{F_t} \tag{9}$$

$$\text{Velocity of mMB} - \text{Ab}: \boldsymbol{v_b} = \boldsymbol{V} + \frac{\boldsymbol{F_m}}{6\pi\mu r_b} \tag{10}$$

$$\text{Particle relaxation time}: \tau = \frac{m_b}{6\pi\mu r_b} \tag{11}$$

$$\text{CE}\,(\%) = \frac{\text{No. of mMB} - \text{Ab captured by magnet}}{\text{No. of mMB} - \text{Ab injected in channel}} \times 100 \tag{12}$$

where $\boldsymbol{B}$ represents the magnetic field intensity, $\boldsymbol{M}$ is the magnetization of NdFeB material, χ is the susceptibility of the mMB-Ab, $\boldsymbol{F_m}$ is the magnetic force, μ_0 is magnetic permeability of vacuum, μ_r is relative permeability of NdFeB material, $\boldsymbol{F_d}$ is the viscous drag force on the mMB-Ab, $\boldsymbol{v_b}$ is the mMB-Ab velocity, r_b is the mMB-Ab radius, ρ_b is the mMB-Ab density, and m_b is the mass of the mMB-Ab. Using Eqs. (7)–(10), the velocity of the mMB-Ab under the effect of the EOF and magnetic fields was calculated. Only the magnetic and flow fields have an impact on the mMB-Ab. Neither the E nor its gradient have any significant effect on them because the mMB-Ab has no electrical charge.

Surface Reaction. For the chemical reaction at the capture zone, a biomolecular, irreversible reaction with a forward rate constant, k_f, and a negligible backward rate constant, k_r, were considered. First, the Ag was transported by diffusion and convection in the presence of EOF toward the capture zone. The Ag transport mass equation is formulated by Eq. (13). Then, it binds with the immobilized mMB-Ab at the capture zone. Hence, the mMB-Ab:Ag complex was formed according to Eq. (14). Equations (15)–(17) depict the consumption of Ag and mMB-Ab, and the formation of mMB-Ab:Ag complex according to the Langmuir–Hinshelwood adsorption [33,34]

$$\frac{D[\text{Ag}]}{Dt} = \mathfrak{D}\nabla^2[\text{Ag}] \tag{13}$$

$$[\text{Ag}] + [\text{mMB} - \text{Ab}] \rightarrow [\text{mMB} - \text{Ab}: \text{Ag}] \tag{14}$$

$$\frac{\partial[\text{Ag}]}{\partial t} = -k_f[\text{Ag}]\{[\text{mMB} - \text{Ab}] - [\text{mMB} - \text{Ab}: \text{Ag}]\} + \text{k}_\text{r}[\text{mMB} - \text{Ab}: \text{Ag}] \tag{15}$$

$$\frac{\partial[\text{mMB} - \text{Ab}]}{\partial t} = -k_f[\text{Ag}]\{[\text{mMB} - \text{Ab}] - [\text{mMB} - \text{Ab}: \text{Ag}]\} + \text{k}_\text{r}[\text{mMB} - \text{Ab}: \text{Ag}] \tag{16}$$

$$\frac{\partial[\text{mMB} - \text{Ab}: \text{Ag}]}{\partial t} = k_f[\text{Ag}]\{[\text{mMB} - \text{Ab}] - [\text{mMB} - \text{Ab}: \text{Ag}]\} - \text{k}_\text{r}[\text{mMB} - \text{Ab}: \text{Ag}] \tag{17}$$

where [Ag] is the concentration of Ag, $\mathfrak{D}$ $(= 1 \times 10^{-10}\ \text{m}^2/\text{s})$ is the diffusion coefficient of Ag, [mMB-Ab] is the concentration of the immobilized mMB-Ab, and [mMB-Ab: Ag] represents the concentration of mMB-Ab:Ag at the capture zone. The k_f and k_r are the respective rate constants for association and dissociation.

Boundary Conditions. The boundary conditions for the EOF and the magnetophoretic flow were used from a previous publication of this lab [14]. The inlet was set to the applied E in the range of 150 V/cm–450 V/cm and the outlet was set to ground. For the flow equations, the computational model is greatly simplified if one does not have to solve the velocity field in the electrical double layer. This situation may be avoided when the thickness of the electrical double layer, known as Debye layer, is small relative to the channel height and width. The Debye layer thickness λ_D is [35]

$$\lambda_D = \left(\frac{3.04}{zM^{\frac{1}{2}}}\right) \times 10^{-10} \tag{18}$$

where z is the valence of the ion(s) and M is molarity (mol/L). For example, for 20 mM phosphate buffer and $z = +1$ (or whatever number is relevant for this investigation), λ_D is 2.15 nm and ${\lambda_D}/{W} = 2.15 \times 10^{-3}$, which is negligible. Thus, a slip boundary condition can be applied on the walls of the microchannel with minimal impact on the accuracy of the flow solution. We refer to Dutta et al. [36] and Dasgupta et al. [37] according to which a slip flow at the boundary can be imposed to approximate the effect of the charged layer. The Debye layer thickness was set to 0.1 μm and the zeta-potential was set to −95.6 mV. The velocity of EOF is calculated from the Helmholtz-Smoluchowski (H–S) equation (Eq. (19)) [38]

$$U_e = -\frac{\zeta\varepsilon E}{\mu} \tag{19}$$

where U_e is the velocity (m/s) of EOF, ε is the permittivity of fluid (C/V.m), and ζ is the zeta potential (V) applied at the microchannel walls as a boundary condition to calculate the potential at the wall. The magnetic field was calculated from the input values of intrinsic mMB-Ab susceptibility (χ) equal to 1.42, and magnetic coercive field (H_c) of the permanent NdFeB magnet equal to 9.79×10^5 A/m. The list of parameters used in the numerical calculations is shown in Table 1.

The inlet concentration of the Ag was an adjustable constant in the range of 0.001 M–1000 M. A representative case of 100 M was

Table 1 List of properties used in numerical calculations

Parameter	Value	Parameter	Value
Fluid density (ρ)	997 kg/m^3 [24]	Radius of mMB (r_b)	1.42 μm [14]
Dynamic viscosity (μ)	8.6×10^{-4} Pa.s [24]	Density of mMB (ρ_b)	1800 kg/m^3 [14]
Relative permittivity (ε_r)	78.8 [39]	Susceptibility (χ)	1.42 [14]
Zeta potential (ζ)	−95.6 mV [39]	Magnetic coercive field (H_c)	9.79×10^5 kg/m^3 [14]
Debye-layer thickness (λ_D)	0.1 μm [14]	Rate constant (k_f)	10^7 L mol^{-1} s^{-1} [23]
EOF electric field	150–450 V/cm [38]	Antigen concentration	0.001–1000 M

Table 2 Normalized surface density of mMB-Ab for different *E* at the capture zone

Electric field (V/cm)	mMB-Ab injected	mMB-Ab captured	Normalized surface density of mMB-Ab
150	20	20	1
275	20	13	0.65
450	20	9	0.45

presented in detail. At the outlet, a concentration of zero was applied. Based on previous data [14], a normalized surface density of the mMB-Ab is specified at the capture zone following the captured mMB-Ab (Table 2). The normalized surface densities of immobilized mMB-Ab for E of 150 V/cm, 275 V/cm, and 450 V/cm are 1, 0.65, and 0.45, respectively. For instance, when 20 mMB-Ab were injected into the microchannel for E of 275 V/cm, 13 mMB-Ab were captured. Hence, the normalized surface density was 0.65 (= 13/20). The rate constant related to the association was 10^7 M^{-1}s^{-1}. The present numerical analysis is convection and reaction dominated in comparison to diffusion. The Peclet number for this study is of order 10^3. The initial value of the Ag concentration was set to zero.

Numerical Method. First, the velocity field in the microchannel was determined using the modified Navier–Stokes equation (Eq. (2)), which included the Coulomb force due to the applied E (Eq. (3)). The magnetic field was solved using the magnetostatic equation (Eq. (6)) [14]. The converged solution of velocity and magnetic fields was then used to compute the magnetic force and

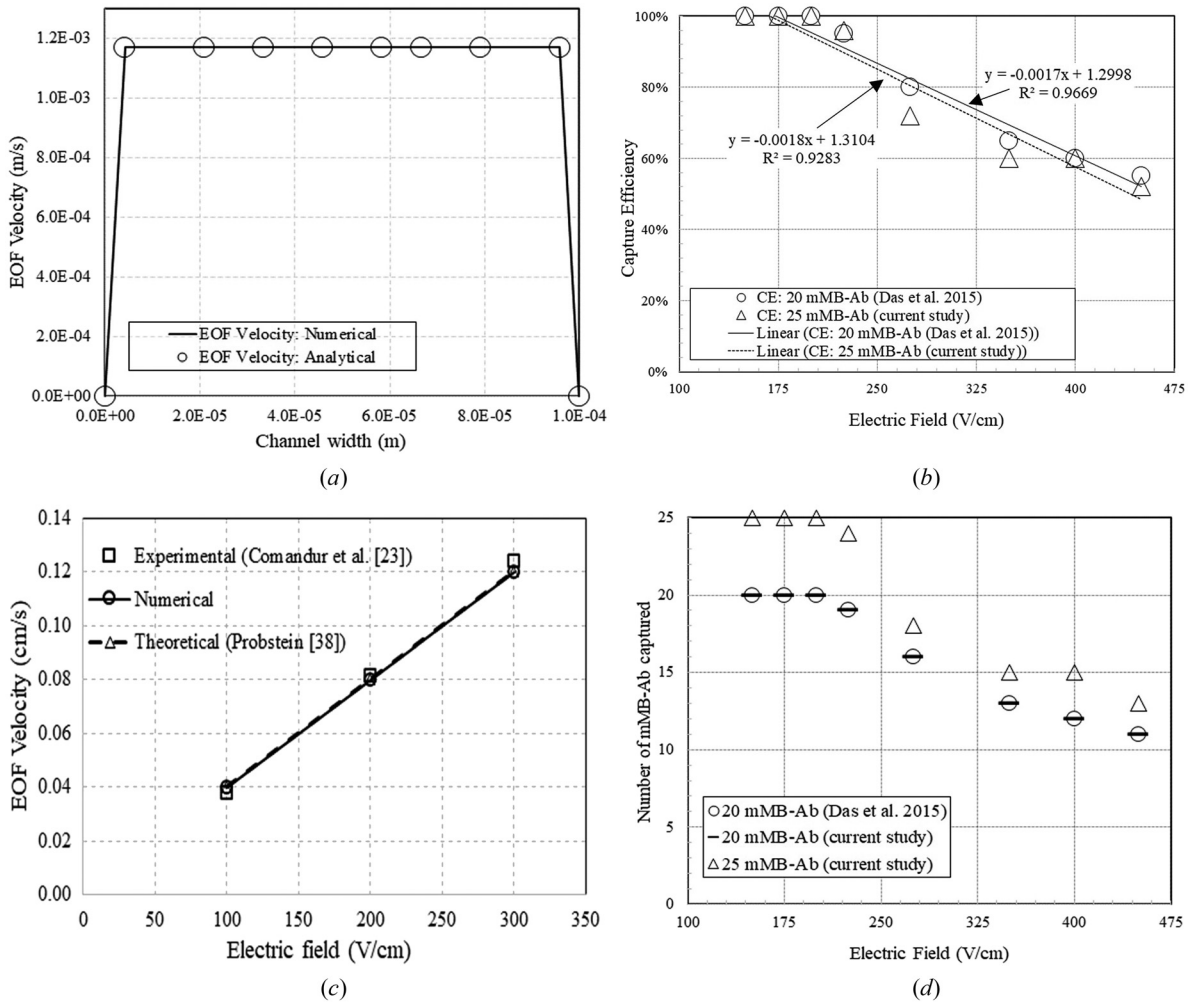

Fig. 2 (*a*) Comparison of numerically and analytically (H–S equation) calculated EOF velocity profiles at an *E* of 150 V/cm, (*b*) CE of mMB-Ab for EOF for different *E*, (*c*) number of mMB-Ab captured at different *E*, and (*d*) Numerical and experimental results indicating the effects of *E* on EOF induced velocity

drag force on the mMB-Ab. The mMB-Ab were captured and immobilized at the capture zone. Afterward, a defined mMB-Ab surface density (Table 2) was used to quantify the amount of immobilized mMB-Ab in the capture zone. Finally, the convection-diffusion equations of the Ag (Eq. (13)) were coupled and solved with the surface reaction (Eq. (14)) between the immobilized mMB-Ab and the Ag at the capture zone. The computation was time-dependent, and the mMB-Ab:Ag complex remained immobilized at the capture zone where it was not carried away from the surface by convection or diffusion.

Validation. To demonstrate grid dependency of the analysis, the EOF velocity profile for an E of 150 V/cm for four mesh configurations having (1) 8910, (2) 19,650, (3) 36,000, and (4) 56, 523 cells was evaluated. Grid-independent results obtained for the mesh configuration (3) (36,000 nodes, mesh size 3.5 μm) were used for the numerical computations.

Velocity Profile of Electro-Osmotic Flow. The analytical solution using H–S equation (Eq. (18)) of steady-state velocity (U_e) of EOF correlates with the magnitude of EOF velocity (Eq. (2)) for the applied E, zeta potential of the channel wall (ζ), fluid permittivity (ε) and viscosity (μ). Figure 2(*a*) shows that the numerical solution for an applied E of 150 V/cm agreed within 0.1% of the analytical velocity profile of EOF calculated by H–S equation.

Immobilization of mMB-Ab. Figure 2(*b*) compares the CE within the microchannel inlet for the injection of 25 mMB-Ab with the injection of 20 mMB-Ab [14] for various E values. As the E increased, the CE decreased. The increase in U_e at higher E resulted in a decrease in CE. The average CE at lower E (150–200 V/cm) was 100% when 20 mMB-Ab and 25 mMB-Ab were injected into the microchannel. However, compared to the injection of 20 mMB-Ab, the CEs for 25 mMB-Ab were 5% ($=100 \times (80_{20\,\text{mMB-Ab}}–76_{25\,\text{mMB-Ab}})/80_{20\,\text{mMB-Ab}}$) and 2.6% ($=100 \times (57.5_{20\,\text{mMB-Ab}}–56_{25\,\text{mMB-Ab}})/57.5_{20\,\text{mMB-Ab}}$) lower for intermediate (225–350 V/cm) and higher (400–450 V/cm) E values, respectively. Therefore, the outcomes of the 25 mMB-Ab injection were comparable to those of the 20 mMB-Ab injection by Das et al. [14].

Figure 2(*c*) shows a similar trend for the quantity of mMB-Ab captured for both 20 mMB-Ab and 25 mMB-Ab injections. As anticipated, the number of mMB-Ab captured decreased with an increase in the E. The current study used 20 mMB-Abs, as also reported in our previous study by Das et al. [14]. Additionally, the 25 mMB-Abs case is to further verify the consistency of the numerical formulation in relation to the increased capture of mMB-Abs.

Figure 2(*d*) shows the numerical and experimental EOF velocities at E ranging from 100 to 300 V/cm. The experiment was performed for three voltages (100 V, 200 V, and 300 V) [23] and the numerical data is compared with these voltages. As shown in Table 3, the EOF-

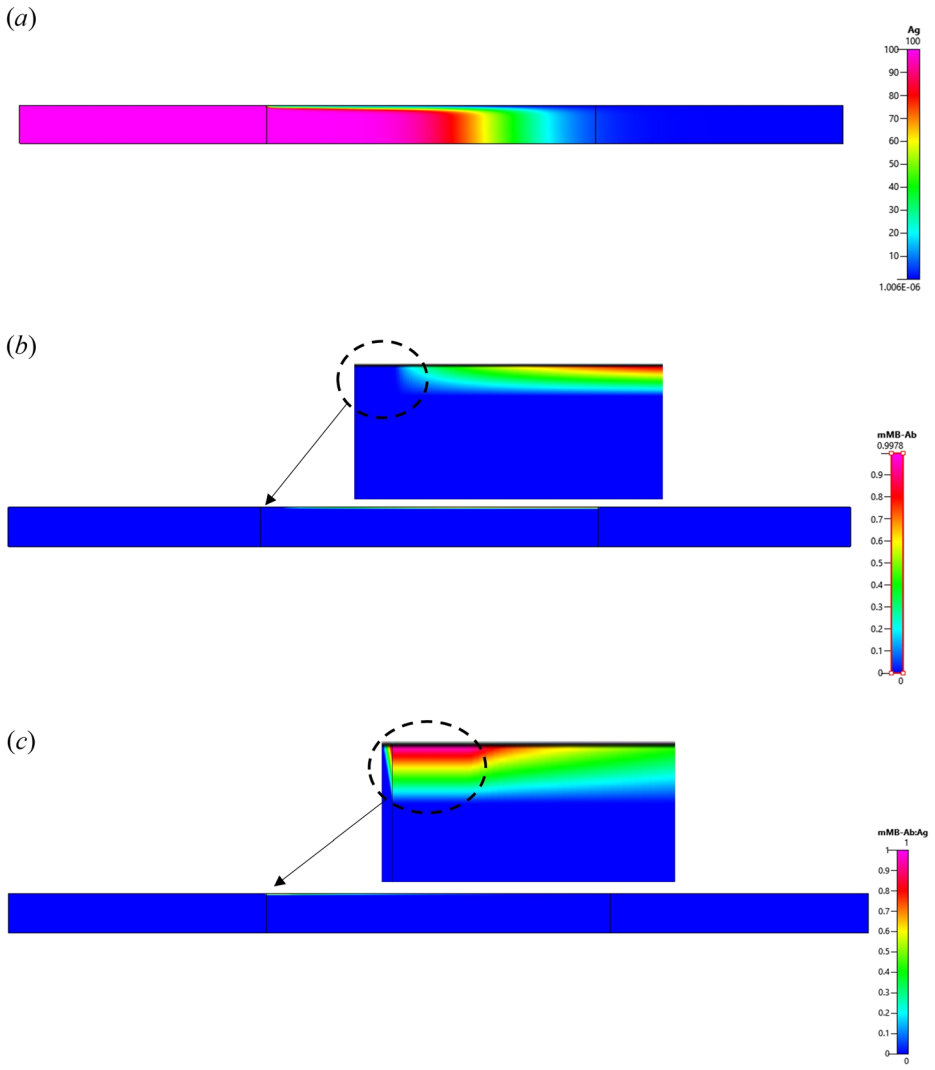

Fig. 3 Contour plots of species: (*a*) Ag, (*b*) mMB-Ab, and (*c*) mMB-Ab-Ag at $t = 1$ s, for an *E* of 150 V/cm

induced velocities indicate a reasonable agreement, within about 6% [=(0.0399–0.0376)/0.0399]. Theoretical prediction using H–S equation (Eq. (19)) [38] has also been added in Fig. 2(*d*).

Results

This section reports the surface reaction between the reactants: (a) immobilized mMB-Ab and (b) the EOF driven Ag in the microchannel. Initially, the depletion of immobilized mMB-Ab and formation of the product: mMB-Ab:Ag complex at the inner wall of microchannel capture zone are presented using representative contour plots. Figure 3 shows the contour plot of the Ag, mMB-Ab, and mMB-Ab:Ag at 1 s for an E of 150 V/cm. Subsequently, the influence of E and Ag concentration on mMB-Ab:Ag formation is investigated.

Depletion of mMB-Ab (Reactant) and Formation of mMB-Ab:Ag (Product).

Spatial Distribution. Figure 4 presents the spatial plot of the normalized surface density of mMB-Ab and mMB-Ab:Ag for an E of 150 V/cm at 0.6 s, 1 s, and 1.6 s. The y-axis shows the normalized surface density of mMB-Ab and mMB-Ab:Ag, and the x-axis shows the length (mm) of the capture zone. As an initial step, the mMB-Ab was captured and immobilized using EOF exposed to magnetic field at the capture zone before Ag was injected into the inlet of microchannel (Fig. 1). The surface densities for mMB-Ab remain fixed at a value of 1.0 for $E = 150$ V/cm. It may be noted that the mMB-Abs were immobilized as an initial step, and the surface density decreased with an increase in E (Table 2). At time $t = 0.6$ s, the initial immobilized mMB-Ab reacted with Ag to form the mMB-Ab:Ag complex till 0.012 mm from the leading edge of the capture zone, (Fig. 4; arrow #I and #1). Similarly, at time $t = 1.6$ s, mMB-Ab:Ag complex was formed till 0.26 mm from the leading edge of the capture zone (Fig. 4; arrow #II and #2). With increase in time, the depletion of mMB-Ab enhances (arrow #III), and the formation of mMB-Ab:Ag (arrow #3) enhances axially (left to right) along the capture zone.

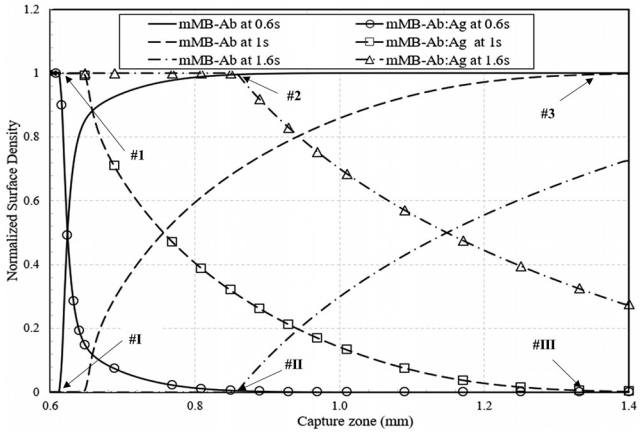

Fig. 4 Spatial plot of normalized surface density of mMB-Ab and mMB-Ab:Ag for an *E* of 150 V/cm at *t* = 0.6 s, 1 s, and 1.6 s, Ag concentration = 100 M

Table 3 Numerical and experimental EOF velocities at E ranging from 100 to 300 V/cm

Electric field (V/cm)	Velocity (experimental, cm/s) Comandur et al. [23]	Velocity (numerical, cm/s)	% Difference
100	0.0376 ± 0.0016	0.0399	6.3
200	0.0811 ± 0.0014	0.0799	1.4
300	0.1238 ± 0.0025	0.1199	3.2

Temporal Distribution. Figure 5 shows the temporal plot of the normalized concentration of Ag, and the normalized surface density of mMB-Ab and mMB-Ab:Ag for an E of 150 V/cm. The left *y*-axis shows the normalized concentration of Ag, the right *y*-axis shows the normalized surface density of mMB-Ab and mMB-Ab:Ag, and the *x*-axis shows the time in seconds. Figures 5(*a*)–5(*c*) show the results at the leading edge ($x = 0.6$ mm), midpoint ($x = 1.0$ mm), and trailing edge ($x = 1.4$ mm) of the capture zone, respectively. Figure 5(*a*) shows that the mMB-Ab was available for the first 0.2 s. However, the mMB-Ab began to deplete once the Ag reached the capture zone after 0.2 s, and was completely depleted after 0.6 s. The reduction in mMB-Ab is due to the formation of mMB-Ab:Ag complex which begins to form after 0.2 s and becomes immobilized at the capture zone by 0.6 s. This indicates successful capture of the Ag.

The results presented in Figs. 5(*b*) and 5(*c*) demonstrate a consistent trend with the finding of Fig. 5(*a*). It is evident that the mMB-Ab remained immobilized at the capture zone until the arrival

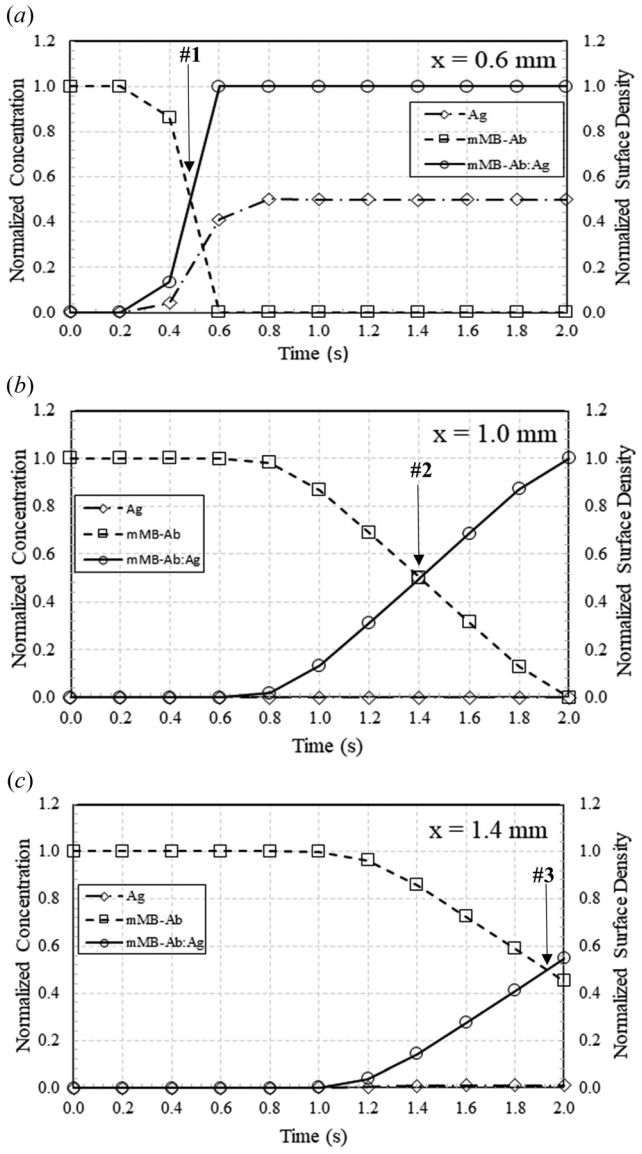

Fig. 5 Temporal plot of Normalized concentration of Ag, surface density of mMB-Ab, and mMB-Ab:Ag at (*a*) leading edge, (*b*) middle, and (*c*) trailing edge of the capture zone for an *E* of 150 V/cm and Ag concentration = 100 M

of the Ag, which then depletes the mMB-Ab over time. Simultaneously, the formation of mMB-Ab:Ag can be observed. The depletion of the mMB-Ab occurred later for the midpoint (Fig. 5(*b*)) and trailing edge (Fig. 5(*c*)) in comparison to the leading edge (Fig. 5(*a*)). The delay is because of the Ag's late arrival progressively at the midpoint and at the trailing edge of the capture zone. The overall magnitude of the Ag is relatively lower and not noticeable at the capture zone in Figs. 5(*b*) and 5(*c*). This is because any free Ag near the wall reacts immediately with the mMB-Ab on the wall, resulting in a near-zero concentration of the Ag at the vicinity of the wall region while mMB-Ab does exist noticeably. The surface reaction between mMB-Ab and Ag shifts from the leading edge (left) to the trailing edge (right) of the capture zone (Fig. 5 (arrow #1 (0.5 s), arrow #2 (1.4 s), and arrow #3 (1.9 s)).

Figures 6(*a*)–6(*d*) show results for Ag concentration of 0.1 M–100 M at the leading edge of the capture zone. The depletion of mMB-Ab and formation of mMB-Ab:Ag follows a similar trend reported in Fig. 5(*a*). The surface density of the immobilized mMB-

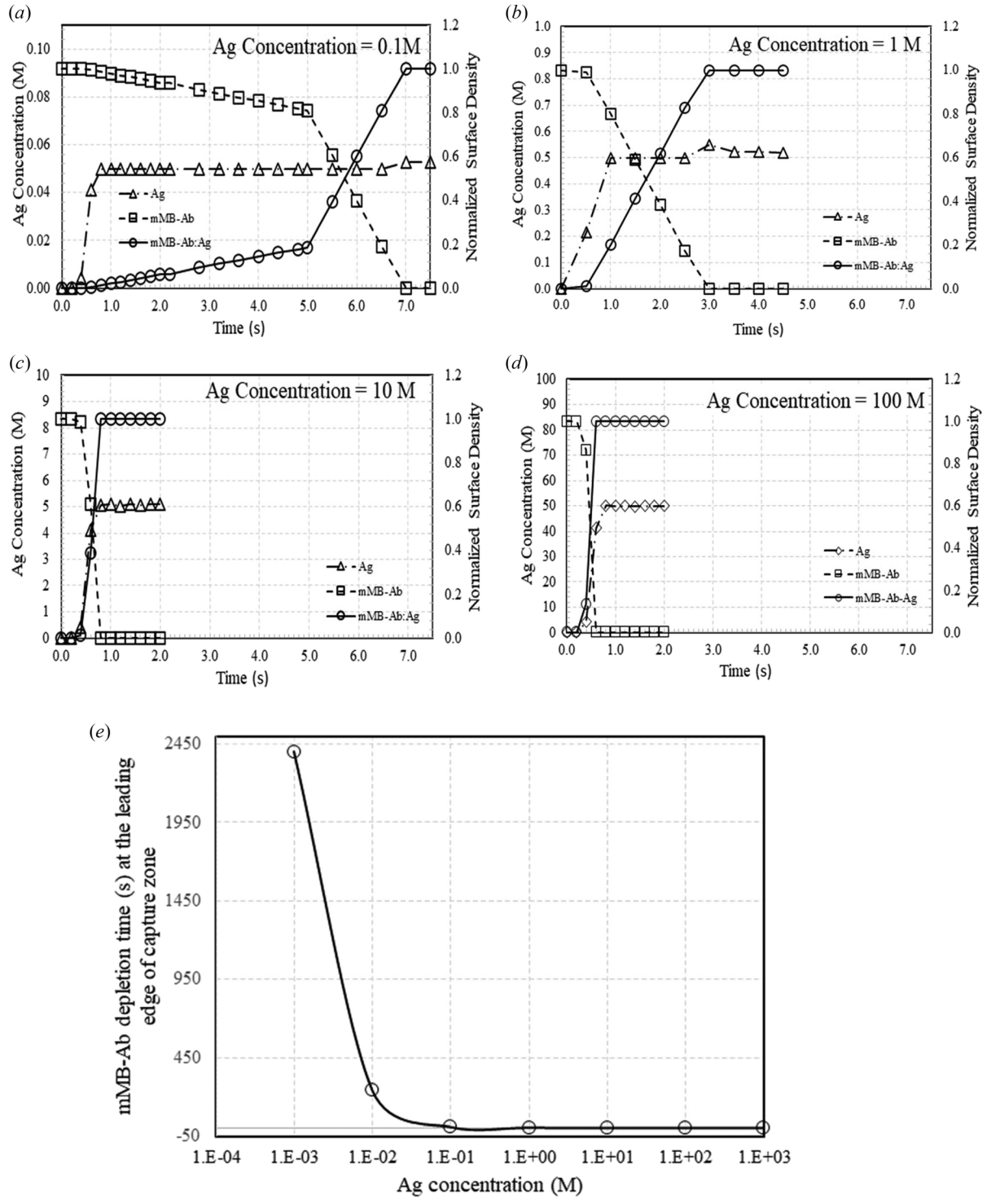

Fig. 6 Temporal plot of Ag concentration, surface density of mMB-Ab, and mMB-Ab:Ag at the leading edge for an Ag concentration of (*a*) 0.1 M, (*b*) 1 M, (*c*) 10 M, and (*d*) 100 M for an E of 150 V/cm, and (*e*) numerical results indicating the effect of Ag concentration on mMB-Ab depletion time at the leading edge of capture zone for an $E = 150$ V/cm

Ab remains the same at the capture zone and began to deplete once the Ag reached the capture zone. Figure 6(*e*) is a composite figure of Figs. 5(*a*) and 6(*a*)–6(*d*). A nonlinear relationship was observed between Ag concentrations (0.001 M–1000 M) and mMB-Ab depletion time at the leading edge of the capture zone. At a lower Ag concentration of 0.001 M, the mMB-Ab:Ag depletion time was 2400 s and rapidly decreased to 240 s at Ag concentration of 0.01 M. Furthermore, it decreases progressively from 7 s to 0.4 s respectively for Ag concentration of 0.1 M–1000 M. These results provide quantifiable data for the detection of Ag, highlighting its potential for rapid throughput screening of Ag.

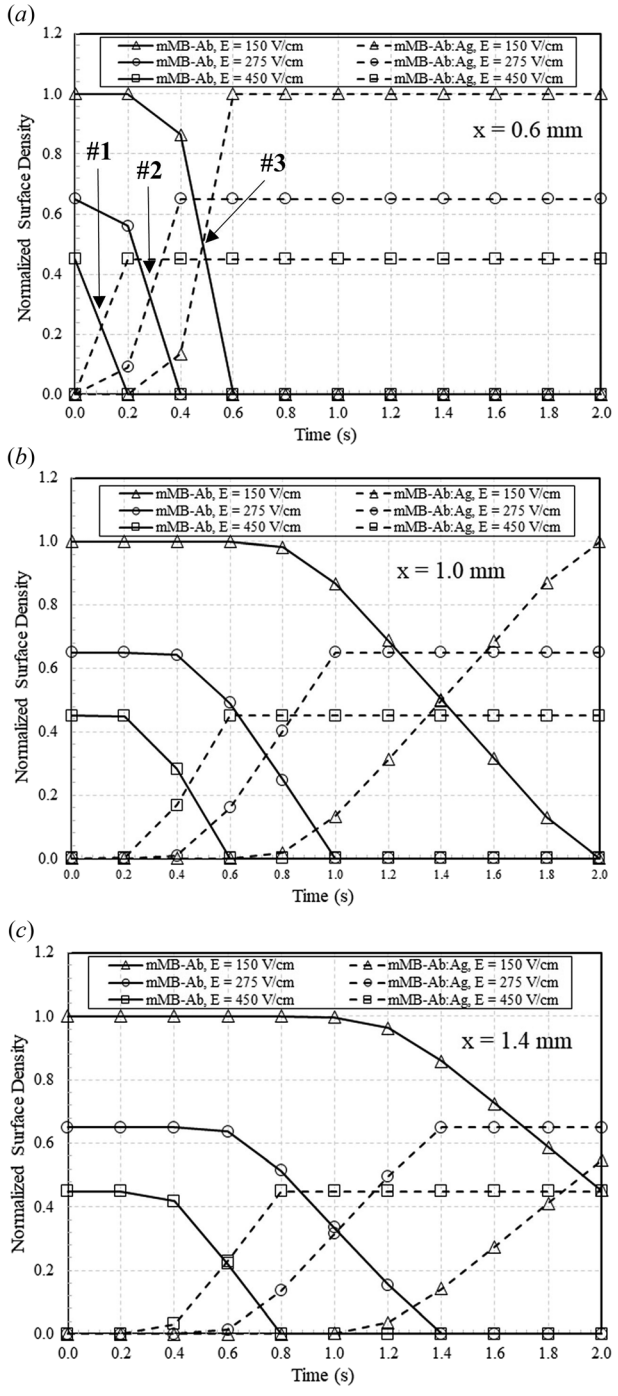

Fig. 7 Normalized surface density of mMB-Ab and mMB-Ab:Ag at (*a*) leading edge ($x = 0.6$ mm), (*b*) middle ($x = 1.0$ mm), and (*c*) trailing edge ($x = 1.4$ mm) of the capture zone for *E* of 150 V/cm, 275 V/cm, and 450 V/cm for Ag concentration = 100 M

Effect of Electric Field (E). The normalized surface densities of mMB-Ab and mMB-Ab:Ag for E of 150 V/cm, 275 V/cm, and 450 V/cm are shown in Fig. 7. The y-axis shows the normalized surface density, whereas the *x*-axis shows the time in seconds. Figures 7(*a*)–7(*c*) show the results at the leading edge ($x = 0.6$ mm), midpoint ($x = 1.0$ mm), and trailing edge ($x = 1.4$ mm) of the capture zone, respectively. Figure 7(*a*) shows the depletion of mMB-Ab and formation of mMB-Ab:Ag for E of 450 V/cm and 275 V/cm along with 150 V/cm (Fig. 5(*a*)). The immobilized mMB-Ab gets depleted when Ag reaches the capture zone. The mMB-Ab gets depleted at $t = 0.2$ s, 0.4 s, and 0.8 s for an *E* of 450 V/cm, 275 V/cm, and 150 V/cm, respectively (Fig. 7(*a*)). These times correspond to times when the mMB-Ab:Ag forms at the microchannel wall of the capture zone. The time to form immobilized mMB-Ab:Ag increases with a decrease in E value. The decrease in the E results in a reduction of the velocity of EOF, leading to a delay in time for the depletion of mMB-Ab. Also, the normalized surface density of mMB-Ab available at the capture zone for depletion decreases with an increase in E as in Fig. 7(*a*) (arrow #1, #2, and #3) and Table 2 last column. This is because immobilized mMB-Ab at microchannel wall, before the injection of Ag, varied inversely proportional to the E, as revealed in Fig. 2(*c*). Figures 7(*b*) and 7(*c*) demonstrate a similar trend as in Figs. 5(*b*) and 5(*c*), where the depletion of mMB-Ab occurred later as Ag reached the midpoint and trailing edge of the capture zone.

Effect of Ag Concentration. Figure 8 shows the normalized surface density of mMB-Ab and mMB-Ab:Ag at the middle of the capture zone for different Ag concentrations of 1 M, 10 M, 100 M, and 1000 M. The *y*-axis represents the normalized surface density of mMB-Ab and mMB-Ab:Ag, and the x-axis is time in seconds. Figure 8 shows that the depletion of mMB-Ab, and formation of mMB-Ab:Ag is similar to the trend seen in Fig. 5(*b*). Figures 8(*a*) and 8(*b*) show the results for the *E* of 150 V/cm and 450 V/cm, respectively. The mMB-Ab got depleted at $t = 1.0$ s and 2.0 s for an Ag concentration of 1000 M and 100 M respectively (Fig. 8(*a*)). The depletion of mMB-Ab (arrow #3 and #4) for an Ag concentration of 10 M and 1 M, respectively, occurs later (beyond $t = 2.0$ s and not shown in the plot). This implies that the depletion of mMB-Ab and formation of mMB-Ab:Ag complex increases with time as Ag concentration decreases. A similar trend was seen in Fig. 8(*b*). The depletion of mMB-Ab occurred at $t = 0.4$ s and 0.6 s for Ag concentrations of 1000 M and 100 M, respectively. The reduction in time is due to an increase in EOF as E increases. Figure 8(*a*) (arrow #1 and #2) and 8B (arrow #I, #II, and #III) show that the surface reaction shifts from left to right as Ag concentration decreases.

Discussion

The current EOF driven microfluidic device eliminates the need for mechanical pumps and provides finer control over media velocity, sample volume, and sample handling automation. In contrast, most pressure-driven microfluidic devices employ external pumps such as syringes to drive the samples. This pressure-driven devices operate at a high pressure that are prone to leakages. Additionally, the plug profile of EOF ensured that the Ag injected into the charged microchannel were uniformly distributed. This study showed that the reaction shifts from the leading edge axially along the capture zone as the Ag reaches the surface consuming the immobilized mMB-Ab on microchannel surface.

Surface Reaction. A significant decrease in depletion time of mMB-Ab was seen as the E increased from 150 V/cm to 450 V/cm. This observation was corroborated by the findings of Kaziz et al. [26]. They observed a reduction in the biosensor response time in detection of COVID 19 virus when the E was increased. The velocity of EOF is directly proportional to the applied E; therefore, an increased E or velocity will hasten the transport of the Ag toward the capture zone leading to quicker detection. Although a faster detection of the Ag is desired, transporting media at a higher E

could lead to Joule heating, resulting in increased dispersion of the Ag due to thermal diffusion across channel width [40]. Contrary, lower E would result in weaker EOF, which might not be able to overcome the counteracting inertial and viscous forces. Hence, an optimized value of E in the range of 150 V/cm–450 V/cm was applied to obtain a desired concentration of Ag in the microchannel.

The surface reaction between Ag and mMB-Ab was also calculated at Ag concentrations of 1 M, 10 M, 100 M, and 1000 M. The depletion time of mMB-Ab increased as Ag concentration decreased (Fig. 8). This is expected because the affinity of the immobilized mMB-Ab is important in the detection of Ag and development of the mMB-Ab:Ag complex. Consequently, increased Ag concentration would aid in overcoming delay in time for detection.

According to the law of mass action

$$\frac{[\text{mMB} - \text{Ab}: \text{Ag}]}{[\text{mMB} - \text{Ab}] \times [\text{Ag}]} = \frac{k_f}{k_r} = K_{\text{eq}}$$

At equilibrium, the concentration ratio of mMB-Ab:Ag to the reactants (mMB-Ab and Ag) is constant. The equilibrium constant, K_{eq}, is equal to the ratio of the rate constants of association (k_f) and dissociation (k_r). To enhance Ag detection, the ratio of mMB-Ab:Ag to mMB-Ab, i.e., $\left(\frac{[\text{mMB}-\text{Ab:Ag}]}{[\text{mMB}-\text{Ab}]}\right)$ should be optimized. As a result, the equation above becomes

$$\frac{[\text{mMB} - \text{Ab}: \text{Ag}]}{[\text{mMB} - \text{Ab}]} = K_{\text{eq}} \times [\text{Ag}]$$

To improve Ag detection, the equilibrium constant or the concentration of Ag needs to be increased. If the Ag is diluted by adding media fluid without changing the temperature, *p*H, or ionic strength while the K_{eq} is constant, then the mMB-Ab:Ag complex would dissociate proportionately, leading to weaker detection of Ag [41]. Furthermore, the influence of dilution is substantially larger for low affinity Ab. It is apparent that the aspect of binding between the immobilized mMB-Ab and Ag in the presence of EOF will need further evaluation in future.

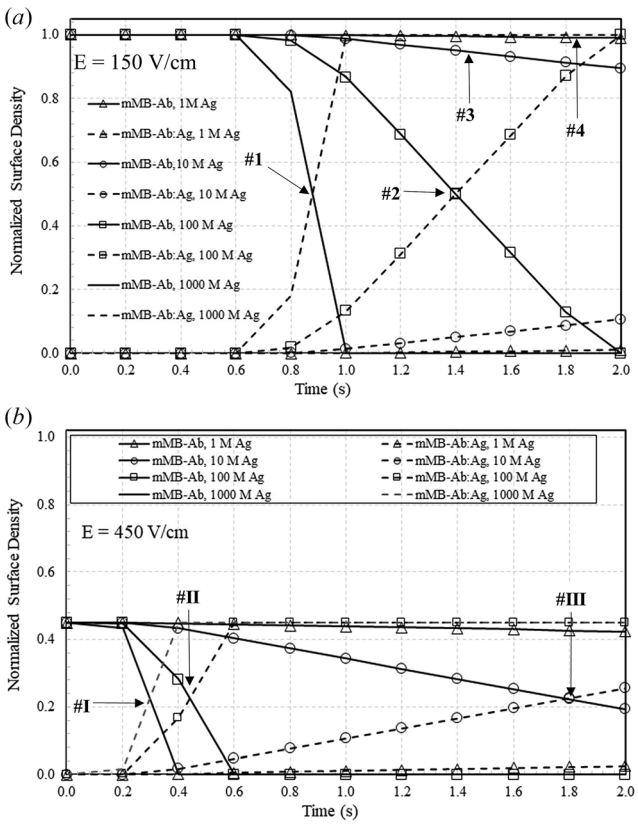

Fig. 8 Normalized surface density of mMB-Ab, and mMB-Ab:Ag at the middle of the capture zone for an E of (*a*) 150 V/cm; and (*b*) 450 V/cm, for different Ag concentrations of 1 M, 10 M, 100 M, and 1000 M

Assumptions and Limitations. The numerical method assumes that the mMB-Abs are sufficiently small compared to the channel width such that the fluid momentum does not get significantly affected by the presence of the mMB-Ab, thereby considering 1-way coupling where fluid momentum influences the momentum of mMB particles but not otherwise. Also, the mMB-Ab which may have escaped could be captured by weaker magnetic fields due to intrinsic magnetic field generated by any superparamagnetic mMB-Ab when exposed to an external magnetic field. The mMB-Abs were treated as discrete particles without their intrinsic magnetic fields. Particle–particle interactions were not analyzed in the current formulation. This assumption is generally valid for low concentration of particles. Further, the immobilized mMB-Ab were assumed not to ricochet back into the flow field. These assumptions were reported by Das et al. [14]. Also, this study assumed that the zeta potential is uniform on the channel walls. Hence, the effect of nonuniform zeta potential, which can drive a secondary flow and promote surface-hybridization reaction due to magnetic beads in the capture zone, was not accounted for. This can be addressed in future studies. Furthermore, in setting up the surface reaction, the capture zone defining binding site was defined similar to the previous study by Das et al. [14], with a specified normalized surface density representing the immobilized mMB-Ab (Table 2). In other words, Eqs. (1)–(17) could not be simultaneously solved. Instead Eqs. (1)–(12) were solved as a first step, followed by solving Eqs. (13)–(17). We anticipate that these assumptions should not affect the accuracy of the computation.

Despite the above limitations, the surface reaction between immobilized mMB-Ab and freestream Ag was found to be useful for rapid throughput screening of Ag. The optimization of the proposed microfluidic device for specific Ag will help in improved detection of target cells, pathogens, and biomolecules during field testing. While the effects of E and Ag concentrations on the surface reaction of immobilized mMB-Ab and Ag were examined, testing the device for various reaction rates needs to be performed in the future. The present study is a convection and reaction dominated cases. The diffusion dominated cases will need to be investigated in the future.

Conclusions

A numerical analysis was conducted illustrating a novel magneto-EOF technique for the detection of Ag by binding with immobilized mMB-Ab using a miniature magnet. The influence of variable E and Ag concentration has been elucidated. The realistic range of E (150 V/cm–450 V/cm), Ag concentration (0.001 M–1000 M), and surface density of mMB-Ab (0.45 – 1) within a microfluidic device were assessed. As E decreases from 450 V/cm to 150 V/cm, the time for depletion of mMB-Ab increases due to reduction of EOF induced velocity. Also, as the concentration of Ag decreases, the time for depletion of mMB-Ab increases. The technique of immobilizing mMB-Ab for the detection of Ag has a high potential in immunoassays for rapid throughput screening. In conclusion, assessing the surface reaction between mMB-Ab and Ag can enable the fabrication of efficient and portable devices for testing water systems, biological fluids, and biochemicals. The proposed platform technology can be tested a priori using the current method and adopted for realistic devices having various combinations of mMB-Ab(s) and Ag(s) with known reaction rates.

Acknowledgment

The authors would like to thank Applied Materials for extending the license of CFD-ACE+ software (Applied Materials, Santa

Clara, CA), resulting in completion of this analysis. Special thanks to Dr. Fadi Benachour, Dr. Kallol Bera, and Dr. Umesh Kelkar for their generosity in helping move forward this work.

Funding Data

- National Institute for Occupational Safety and Health through the University of Cincinnati Education and Research Center (Grant No. T42OH008432; Funder ID: 10.13039/100000125).

Data Availability Statement

The datasets generated and supporting the findings of this article are obtainable from the corresponding author upon reasonable request.

Nomenclature

Ag = antigen
$\boldsymbol{B}$ = magnetic field strength, Wb/m^2 or T
CE = capture efficiency, %
$\boldsymbol{E}$ = electric field, V/m
EOF = electroosmotic flow
$\boldsymbol{F_d}$ = viscous drag force, N
$\boldsymbol{F_d}$ = gravitational force, N
$\boldsymbol{F_d}$ = Brownian force, N
$\boldsymbol{f_e}$ = Coulomb force, N
$\boldsymbol{F_m}$ = magnetic force, N
k_f = forward rate constant
k_r = backward rate constant
$\boldsymbol{M}$ = magnetization of NdFeB, A/m
m_b = mass of mMB-Ab, kg
mMB-Ab = magnetic microbead-tagged-antibodies
mMB-AbAg = mMB-Ab and Ag complex
NdFeB = neodymium alloy
$\boldsymbol{p}$ = pressure, Pa
r_b = mMB-Ab radius, N
U_e = EOF velocity magnitude, m/s
$\boldsymbol{V}$ = fluid velocity, m/s
$\boldsymbol{v_b}$ = mMB-Ab velocity, m/s
$\mathfrak{D}$ = diffusion coefficient of Ag, m^2/s

Greek Symbols

ε = permittivity, C/V.m
ζ = zeta potential, V
λ_D = debye layer thickness, μm
μ = dynamic viscosity of fluid, Pa·s
μ_0 = magnetic permeability of vacuum, Wb/A.m
μ_r = relative permeability of NdFEB, unitless
ρ = fluid density, kg/m^3
ρ_b = density of mMB-Ab, kg/m^3
ρ_e = bulk charge density, kg/m^3
τ = particle relaxation time, s
φ = applied EOF voltage, V
χ = susceptibility of mMB-Ab, unitless

References

[1] Zhou, X., Hu, Z., Yang, D., Xie, S., Jiang, Z., Niessner, R., Haisch, C., Zhou, H., and Sun, P., 2020, "Bacteria Detection: From Powerful SERS to Its Advanced Compatible Techniques," Adv. Sci., **7**(23), p. 2001739.
[2] Abraha, H. B., Kim, K. P., and Sbhatu, D. B., 2023, "Bacteriophages for Detection and Control of Foodborne Bacterial Pathogens—The Case of Bacillus Cereus and Their Phages," J. Food Saf., **43**(2), p. e12906.
[3] Wang, P., Yu, G., Wei, J., Liao, X., Zhang, Y., Ren, Y., Zhang, C., et al., 2023, "A Single Thiolated-Phage Displayed Nanobody-Based Biosensor for Label-Free Detection of Foodborne Pathogen," J. Hazard. Mater., **443**, p. 130157.
[4] Toyos-Rodríguez, C., García-Alonso, F. J., and de la Escosura-Muñiz, A., 2023, "Towards the Maximization of Nanochannels Blockage Through Antibody-Antigen Charge Control: Application for the Detection of an Alzheimer's Disease Biomarker," Sens. Actuators, B, **380**, p. 133394.
[5] Ahangari, A., Mahmoodi, P., and Mohammadzadeh, A., 2023, "Advanced Nano Biosensors for Rapid Detection of Zoonotic Bacteria," Biotechnol. Bioeng., **120**(1), pp. 41–56.
[6] Pandian, S., Lakshmi, S. A., Priya, A., Balasubramaniam, B., Zaukuu, J.-L. Z., Durgadevi, R., Abe-Inge, V., and Sohn, S.-I., 2023, "Spectroscopic Methods for the Detection of Microbial Pathogens and Diagnostics of Infectious Diseases—An Updated Overview," Processes, **11**(4), p. 1191.
[7] Singh, S., Chandratre, G., and Narang, G., 2023, "Detection of Bacterial Pathogens From the Pneumonic Lungs of Sheep and Goats and Their Antimicrobial Sensitivity Pattern," Proc. Natl. Acad. Sci., India Sect. B, **94**(1), pp. 69–74.
[8] Daniel, F., Kesterson, D., Lei, K., Hord, C., Patel, A., Kaffenes, A., Congivaram, H., and Prakash, S., 2022, "Application of Microfluidics for Bacterial Identification," Pharmaceuticals, **15**(12), p. 1531.
[9] Zhang, D., Bi, H., Liu, B., and Qiao, L., 2018, "Detection of Pathogenic Microorganisms by Microfluidics Based Analytical Methods," Anal. Chem., **90**(9), pp. 5512–5520.
[10] Spatola Rossi, C., Coulon, F., Ma, S., Zhang, Y. S., and Yang, Z., 2023, "Microfluidics for Rapid Detection of Live Pathogens," Adv. Funct. Mater., **33**(21), p. 2212081.
[11] Hong, S.-L., Zhang, M.-F., Wang, X., Liu, H., Zhang, N., Tang, M., and Li, W., 2023, "Magnetic-Based Microfluidic Chip: A Powerful Tool for Pathogen Detection and Affinity Reagents Selection," Crit. Rev. Anal. Chem., pp. 1–12.
[12] Bazaz, S. R., Zhand, S., Salomon, R., Beheshti, E. H., Jin, D., and Warkiani, M. E., 2023, "ImmunoInertial Microfluidics: A Novel Strategy for Isolation of Small EV Subpopulations," Appl. Mater. Today, **30**, p. 101730.
[13] McCloskey, K. E., Chalmers, J. J., and Zborowski, M., 2003, "Magnetic Cell Separation: Characterization of Magnetophoretic Mobility," Anal. Chem., **75**(24), pp. 6868–6874.
[14] Das, D., Al-Rjoub, M. F., and Banerjee, R. K., 2015, "Enhanced Capture of Magnetic Microbeads Using Combination of Reduced Magnetic Field Strength and Sequentially Switched Electroosmotic Flow–A Numerical Study," ASME J. Biomech. Eng., **137**(5), p. 051008.
[15] Min, H., Jo, S. M., and Kim, H. S., 2015, "Efficient Capture and Simple Quantification of Circulating Tumor Cells Using Quantum Dots and Magnetic Beads," Small, **11**(21), pp. 2536–2542.
[16] Lu, N.-N., Xie, M., Wang, J., Lv, S.-W., Yi, J.-S., Dong, W.-G., and Huang, W.-H., 2015, "Biotin-Triggered Decomposable Immunomagnetic Beads for Capture and Release of Circulating Tumor Cells," ACS Appl. Mater. Interfaces, **7**(16), pp. 8817–8826.
[17] You, S.-M., Luo, K., Jung, J.-Y., Jeong, K.-B., Lee, E.-S., Oh, M.-H., and Kim, Y.-R., 2020, "Gold Nanoparticle-Coated Starch Magnetic Beads for the Separation, Concentration, and SERS-Based Detection of E. coli O157: H7," ACS Appl. Mater. Interfaces, **12**(16), pp. 18292–18300.
[18] Meeseepong, M., Ghosh, G., Shrivastava, S., and Lee, N.-E., 2023, "Fluorescence-Enhanced Microfluidic Biosensor Platform Based on Magnetic Beads With Highly Stable ZnO Nanorods for Biomarker Detection," ACS Appl. Mater. Interfaces, **15**(18), pp. 21754–21765.
[19] Lin, Y.-H., Chen, Y.-J., Lai, C.-S., Chen, Y.-T., Chen, C.-L., Yu, J.-S., and Chang, Y.-S., 2013, "A Negative-Pressure-Driven Microfluidic Chip for the Rapid Detection of a Bladder Cancer Biomarker in Urine Using Bead-Based Enzyme-Linked Immunosorbent Assay," Biomicrofluidics, **7**(2), p. 24103.
[20] Yao, S., Hertzog, D. E., Zeng, S., Mikkelsen, J. C., and Santiago, J. G., 2003, "Porous Glass Electroosmotic Pumps: Design and Experiments," J. Colloid Interface Sci., **268**(1), pp. 143–153.
[21] Chen, C.-H., and Santiago, J. G., 2002, "A Planar Electroosmotic Micropump," J. Microelectromech. Syst., **11**(6), pp. 672–683.
[22] Das, D., Al-Rjoub, M. F., Heineman, W. R., and Banerjee, R. K., 2016, "Efficient Capture of Magnetic Microbeads by Sequentially Switched Electro-osmotic Flow—An Experimental Study," J. Micromech. Microeng., **26**(5), p. 055013.
[23] Comandur, K., Bhagat, A. A., Bhagat, S., Dasgupta, S., Papautsky, I., and Banerjee, R., 2010, "Transport and Reaction of Nanoliter Samples in a Microfluidic Reactor Using Electro-Osmotic Flow," J. Micromech. Microeng., **20**(3), p. 35017.
[24] Al-Rjoub, M. F., Roy, A. K., Ganguli, S., and Banerjee, R. K., 2015, "Improved Flow Rate in Electro-Osmotic Micropumps for Combinations of Substrates and Different Liquids With and Without Nanoparticles," ASME J. Electron. Packag., **137**(2), p. 021001.
[25] Selmi, M., and Belmabrouk, H., 2020, "AC Electroosmosis Effect on Microfluidic Heterogeneous Immunoassay Efficiency," Micromachines, **11**(4), p. 342.
[26] Kaziz, S., Saad, Y., Bouzid, M., Selmi, M., and Belmabrouk, H., 2021, "Enhancement of COVID-19 detection Time by Means of Electrothermal Force," Microfluid. Nanofluid., **25**(10), pp. 1–12.
[27] Alipanah, M., Hafttananian, M., Hedayati, N., Ramiar, A., and Alipanah, M., 2021, "Microfluidic on-Demand Particle Separation Using Induced Charged Electroosmotic Flow and Magnetic Field," J. Magn. Magn. Mater., **537**, p. 168156.
[28] Deraney, R. N., Schneider, L., and Tripathi, A., 2020, "Synergistic Use of Electroosmotic Flow and Magnetic Forces for Nucleic Acid Extraction," Analyst, **145**(6), pp. 2412–2419.
[29] Miller, S., Weiss, A. A., Heineman, W. R., and Banerjee, R. K., 2019, "Electroosmotic Flow Driven Microfluidic Device for Bacteria Isolation Using Magnetic Microbeads," Sci. Rep., **9**(1), p. 14228.
[30] Banerjee, R. K., Das, D., and Al-Rjoub, M., 2022, "Enhanced Capture of Magnetic Microbeads in Microfluidic Devices Using Sequentially Switched Electroosmotic Flow," Patent No. 11,260,391.
[31] Miller, S. A., Heineman, W. R., Weiss, A. A., and Banerjee, R. K., 2018, "Analysis of Magnetic Microbead Capture With and Without Bacteria in a Microfluidic Device Under Different Flow Scenarios," ASME J. Med. Devices, **12**(4), p. 041005.

[32] Krishnamoorthy, S., Feng, J., Henry, A., Locascio, L. E., Hickman, J., and Sundaram, S., 2006, "Simulation and Experimental Characterization of Electro-osmotic Flow in Surface Modified Channels," Microfluid. Nanofluid., **2**(4), pp. 345–355.
[33] Berthier, J., and Silberzan, P., 2010, *Microfluidics for Biotechnology*, Artech House, Norwood, MA.
[34] Zimmermann, M., Delamarche, E., Wolf, M., and Hunziker, P., 2005, "Modeling and Optimization of High-Sensitivity, Low-Volume Microfluidic-Based Surface Immunoassays," Biomed. Microdevices, **7**(2), pp. 99–110.
[35] Li, D., 2004, *Electrokinetics in Microfluidics*, Elsevier, Toronto, ON, Canada.
[36] Dutta, P., Beskok, A., and Warburton, T. C., 2002, "Electroosmotic Flow Control in Complex Microgeometries," J. Microelectromech. Syst., **11**(1), pp. 36–44.
[37] Dasgupta, S., Bhagat, A. A. S., Horner, M., Papautsky, I., and Banerjee, R. K., 2008, "Effects of Applied Electric Field and Microchannel Wetted Perimeter on Electroosmotic Velocity," Microfluid. Nanofluid., **5**(2), pp. 185–192.
[38] Probstein, R. F., 2005, *Physicochemical Hydrodynamics: An Introduction*, Wiley, New York.
[39] Al-Rjoub, M. F., Roy, A. K., Ganguli, S., and Banerjee, R. K., 2011, "Assessment of an Active-Cooling Micro-Channel Heat Sink Device, Using Electro-Osmotic Flow," Int. J. Heat Mass Transfer, **54**(21–22), pp. 4560–4569.
[40] Ghosal, S., 2006, "Electrokinetic Flow and Dispersion in Capillary Electrophoresis," Annu. Rev. Fluid Mech., **38**(1), pp. 309–338.
[41] Hughes-Jones, N., Polley, M. J., Telford, R., Gardner, B., and Kleinschmidt, G., 1964, "Optimal Conditions for Detecting Blood Group Antibodies by the Antiglobulin Test," Vox Sang., **9**(4), pp. 385–395.